Aerospace Science and Technology 138 (2023) 108305

Contents lists available at ScienceDirect

Aerospace Science and Technology

journal homepage: www.elsevier.com/locate/aescte

Forced response in a multi-stage aeroderivative axial compressor with acoustic excitations: Method validation with field data

Lorenzo Pinelli [a,*], Corrado Burberi [a], Mirko Ignesti [b], Vittorio Michelassi [b], Libero Tapinassi [b], Alessandro Abati [b], Roberto Pacciani [a]

[a] *Department of Industrial Engineering, University of Florence, Via S. Marta 3, 50139 Florence, Italy*
[b] *Baker Hughes, Via F. Matteucci 2, 50127 Florence, Italy*

ARTICLE INFO

Article history:
Received 12 January 2023
Received in revised form 14 March 2023
Accepted 29 March 2023
Available online 17 April 2023
Communicated by Damiano Casalino

Keywords:
Axial compressor
Aeromechanics
CFD

ABSTRACT

This paper presents the application of a forced response prediction process to an industrial aeroderivative axial compressor and its validation against experimental data. The forced response process is based on a dedicated strategy to decompose the overall unsteady aerodynamic forcing coming from URANS analyses, and an improved use of the interference diagram to detect additional acoustic forcing in the entire operating range. The identification of potential resonance conditions, or crossings, in the interference diagram is based on the assumptions of a cyclic symmetry tuned structure and a forcing function having an aliased engine order driven only by the airfoil count of the rotor/stator interactions of interest. Despite this, it is not rare that unexpected resonances appear during compressor validation tests, often calling for painful and time-consuming redesigns. This is witnessed by the unsteady analysis of an 11-stage axial compressor in which the spatial content of engine order forcing is influenced also by further rotor/stator interactions by means of Tyler-Sofrin acoustic modes that cause the onset of additional crossing conditions.

The theory based on time and space decomposition is validated with full 3D unsteady forced response simulations of the entire multistage compressor. Numerical results, obtained by an in-house modal work approach, are compared with experimental data focusing on two resonances, the first of which can be detected by the classical interference diagram, while the second one is justified only by the improved use that considers the acoustic excitations. In both cases, the predicted blade responses are in good agreement with measurements.

The theory associated with the generation mechanism of the additional nodal diameters is further explained using the results of dedicated numerical experiments conducted by changing the relative stator and rotor airfoil count on a reduced compressor domain.

1. Introduction

Both compressor and turbine design must include the accurate verification of the aeromechanic risks. The so-called Campbell diagram, originally explained and introduced in 1924, verifies if natural and aerodynamic forcing frequencies overlap, with a potential destructive result, while the Goodman diagram, introduced in 1899, addresses the companion fatigue risk. The Campbell diagram alone is not enough to make design decisions as it can indicate more potential problems than problems that actually exist. There is a vast literature that addresses the complex physic behind the unsteady fluid structure interaction in gas turbine engines. Among these, Barankiewicz and Hathaway [1] investigated the fundamental aerodynamic stator-rotor interaction by using a four-stage low speed axial compressor. The authors observed that stator-stator with unequal blade count may produce azimuthal distortions that do require to survey across more than one blade row pitch, as confirmed by the circumferential changes of the pressure coefficient amplitudes that may interact with the corresponding nodal diameters. The authors also scrutinized clocking effects on performance, observing little impact on efficiency. Based upon these, the present paper focuses on aeromechanic forcing and the corresponding aeromechanics risk. Vahdati et al. [2] employed full 3D unsteady multi passage and multirow CFD coupled with structural elements to investigate forced response in a 2.5 stage axial compressor. They revealed the shortcomings of calculations performed on reduced number of rows and, among their most important results, the authors discovered that the excitation of a rotor blade

* Corresponding author.
E-mail address: lorenzo.pinelli@unifi.it (L. Pinelli).

https://doi.org/10.1016/j.ast.2023.108305
1270-9638/

Nomenclature

BPF	Blade Passing Frequency	N	Blade number
DFT	Discrete Fourier Transform	N	Newton
EO	Engine Order	ND	Nodal Diameter
δ_m	Modal displacement	m	Circumferential order
F_a	Aerodynamic forcing	R	Rotor
F_m	Modal force	S	Stator
k	Harmonic or scattering index	ω	Angular frequency
ξ	Damping	Ω	Rotational speed
L	Aerodynamic work		

associated to low-engine orders, that appear when two consecutive stator or rotor rows have a small count difference, may produce high response. Obviously, this is not a risk in presence of clockable consecutive stators. Still, clocking is a double-edge knife as it may offer limited performance improvement opportunities, but it may also amplify aeromechanic risks in case the selected relative position is incorrect.

Terstegen et al. [3] measured the aerodynamic excitation in a 2.5 stage axial compressor. The authors described the physics of Tyler-Sofrin [4] modes and supported their conclusions with CFD simulations with both a linearized and harmonic balance solver version by Frey et al. [5] capable of an excellent match with data also in terms of vibrational stresses and pressure amplitudes and spectra. The measurements revealed spinning azimuthal modes as well as the scattering of these modes due to the interactions with blade rows. The authors also mention that manufacturing deviations cause systematic discrepancies in the measured pressure amplitudes and concluded that acoustic multirow interaction is essential for the accurate prediction of the compressor vibrational stresses. In part II of the same paper, Sanders et al. [6] investigated the impact of CFD modeling choices, like turbulence and transition model and grid convergence, on the predictions. It turned out that the single row linearized approach was unable to get the right answer in terms of response when acoustic modes were a major source of excitation, while the non-linear harmonic method guaranteed a better match with data. The computations also revealed the need of a reliable transition model to guarantee a good match with data.

The complex aero-mechanical coupling across the operability range of axial compressors have been investigated by Baumgartner et al. [7] who analyzed the high vibrations in the first rotor of a high-pressure compressor. The vibrations were caused by a rotating flow instability, similar to rotating stall induced pressure fluctuations, the frequency of which did not match with harmonics of the rotor speed. The comparison between the pressure/velocity fluctuations and the blade vibration confirmed the excitation source. This paper reveals that different source of excitation may arise while moving across the compressor speedline, and this needs to be addressed by extending the aeromechanic check to off-design conditions.

More recently Figaschewsky et al. [8] used a 4.5-stage research axial compressor to investigate the effect of Tyler–Sofrin modes on forced response vibrations. The analysis was supported by unsteady CFD, although with a simplified quasi-2D approach of the full circumference. Both measurements and simulations suggest that mistuning effects may be amplified by the presence of Tyler-Sofrin modes. The paper tackles two operating conditions with different sets of variable stator vanes (VSV) and investigates how damping and modal shapes affect the structural coupling concluding that the computational model provides a fair representation of the physics.

The study of aeromechanical vibration of fans and compressors is thus a challenging task [9] and several recent works also include additional aspects like blade mistuning [10], and low engine order excitations due to boundary layer ingestion [11].

With this in mind, this paper describes how 3D unsteady CFD of an 11-stage axial compressor was used to support the interpretation of aeromechanics measurements taken in a dedicated set of experimental tests. The concerted use of CFD and data indicated a spatial decomposition of the aerodynamic forcing and an improved way to use the interference, or safe, diagram described by Singh et al. [12], and verify its applicability to design and off-design conditions. Experimental data and numerical predictions of the forced response are in good agreement and validate the methodology based on the spatial decomposition of the unsteady forcing.

2. Theory

Forced response analysis is based on theoretical concepts like blade dynamic, forcing definition, damping evaluation, and others. This section describes the fundamentals of the background theory with a special emphasis on the application and interpretation of spatial decomposition applied to unsteady forcing and its implications for verification purposes in the framework of a design activity. A preliminary study of the blade unsteady loading variation along the blade-row suggested the need for this spatial decomposition that follows the concept of mode-shapes in cyclic symmetry. This aspect is further explained by Fig. 1, that shows the blade distribution of the pressure time-Fourier coefficient amplitudes on the blade-row. The plot highlights the circumferential variability of this quantity that deserves a dedicated spatial decomposition to extract the rotating forcing components as described below.

2.1. Modal analysis with cyclic symmetry

Structural dynamic analysis of a compressor row is usually performed on a one-pitch sector model composed by blade plus disk. Centrifugal forces and mean temperature and pressure distributions on the blade surfaces characteristic of the operating point under investigation are applied to the model for the pre-stress analysis. At the single pitch sector tangential cuts, cyclic symmetry conditions are imposed to exploit the row axial symmetry and reduce the computational domain. Thanks to this numerical approach the blade row mode-shapes are represented by traveling waves with a defined nodal diameter ND that are usually collected in mode families conventionally called 1F (1st flex), 1T (1st torsional), etc. The sign of the nodal diameter is usually related to machine rotational direction: positive nodal diameter represents forward traveling wave, while negative values mean backward traveling wave.

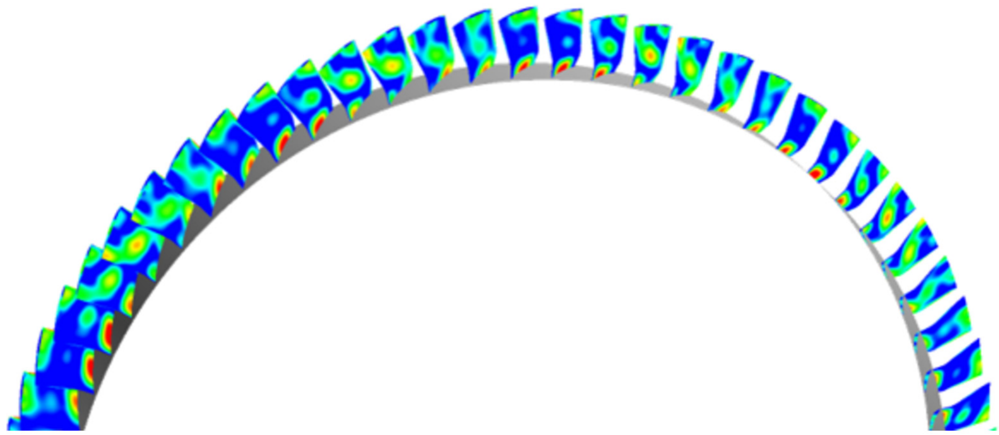

Fig. 1. Amplitude of pressure time Fourier coefficients on adjacent blade surfaces along the blade-row.

2.2. Spatial decomposition and Tyler-Sofrin modes

The decomposition of the unsteady aerodynamic forcing generated by the upstream and downstream airfoil rows is extracted on the analyzed blade-row from a multi-stage full annulus URANS solution [13]. The Discrete Fourier Transform (DFT), applied both in time and in space, allows to extract the pressure fluctuation components in the cyclic symmetry environment. To do this, the time-varying pressure fluctuation seen by an airfoil row is firstly decomposed in time to extract the harmonic content at a single Engine Order (EO) by the following formulation:

$$P^{(h)} = \frac{1}{N_{div}} \sum_{n_t=0}^{N_{div}-1} p_t e^{-ih\frac{2\pi}{N_{div}} n_t} \tag{1}$$

in which h is the time harmonic index (or Engine Order), p_t is the discrete equally spaced pressure signal in time and N_{div} is the total number of samples.

The resulting complex Fourier coefficients $P^{(h)}$ extracted on blade surfaces grid points are further spatially decomposed along the circumferential direction to determine the rotating perturbation that will excite the corresponding traveling wave mode-shape. The time-space Fourier coefficients are extracted along corresponding points on grid surface as follows:

$$\hat{P}^{(h)}_{(m)} = \frac{1}{N} \sum_{k=1}^{N} P^{(h)}_k e^{-im\frac{2\pi}{N} k} \tag{2}$$

in which m is the circumferential order, $P^{(h)}_k$ the discrete time Fourier coefficient tangential distribution on blade corresponding surface points and N the blade count.

The approach that extracts perturbations in space-time (see the spinning lobes in annular ducts as described by Tyler and Sofrin [4]). This is usually employed in aeroacoustics where this circumferential decomposition is performed along the computational grid (instead of along corresponding points on blade surface mesh as in the presented approach) in the annular duct between rows to extract noise components in terms of their acoustic power.

In the present time-space decomposition, the circumferential DFT is thus performed on a coarse down-sampled set of only N samples taken on each blade at corresponding positions (grid points) on the surface. Hence, the extracted rotating pressure components have a number of lobes ranging from $-N/2$ to $+N/2$ or from $-(N-1)/2$ to $+(N-1)/2$ in case of odd blade count as suggested by the Nyquist's theorem. It is clear how this approach also takes into account the aliasing phenomenon experienced by the blade-row when excited by a rotating perturbation with a lobe number higher then $N/2$.

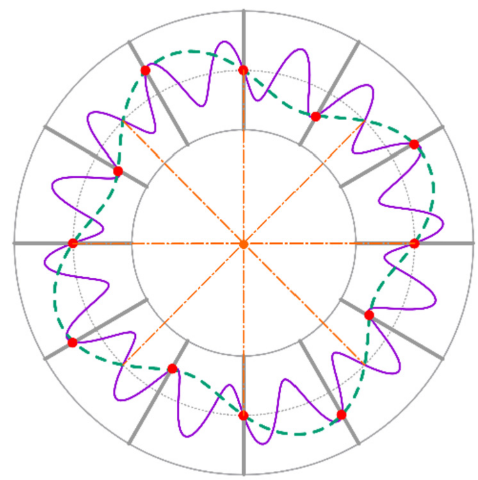

Fig. 2. Sketch of lobe circumferential pattern and aliasing.

Fig. 2 provides a visual representation of a possible excitation scenario, where a rotating perturbation with 16 lobes, represented by the solid line, impinges on a row composed by 12 blades represented by the radial segments. The 12 blades experience a 4-lobe perturbation represented by the dashed-line due to the aliasing phenomenon. The dash-dot radial lines highlight the resulting 4 nodal diameters associated to the 4-lobe excitation. The proposed spatial decomposition on "blade-sampled" corresponding N points along the circumferential direction is thus able to convert the 16-lobe incoming perturbation into the 4-lobe excitation experienced by the blade-row which will finally vibrate as a traveling wave with 4 nodal diameters.

Therefore, it is essential to evaluate all the possible rotating lobes that compose a single engine order perturbation: each spinning lobe can be seen as direct or aliased excitations for the blade-row. Tyler and Sofrin [4] theory states that rotor-stator interactions generate pressure spinning lobes, that are in fact acoustic waves, which travel along the machine causing additional "acoustic excitations" for a given blade-row. The concept of Tyler and Sofrin modes is thus employed to decompose the overall perturbation. The resulting rotating lobes perturbation predicted by theory are included in the improved use of the interference diagram to detect any further possible crossing. The theory presented here is a generalization with different rotational speeds (see Fig. 3) of the original Tyler and Sofrin formulation and it includes propagation

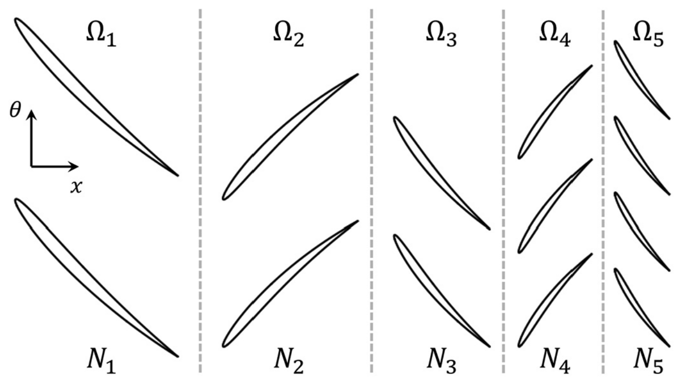

Fig. 3. Blade-to-blade sketch.

effects and further scattering by previous or successive blade-rows [14].

The generalized rotor-stator interaction theory predicts the generation of rotating perturbations with the number of lobes m (i.e. the circumferential order) and angular frequency ω in the different frames of reference (fixed or rotating with rotational speed Ω and defined by the subscripts from 1 to 5). For instance, with reference to Fig. 3, the pressure rotating lobes in the frame of reference of the blade-row 2 are characterized by:

$$\begin{aligned} m_2 &= k_1 N_1 - k_2 N_2 \\ \omega_2 &= k_1 N_1 (\Omega_1 - \Omega_2) \end{aligned} \tag{3}$$

where N is the blade count and k is an integer value called harmonic or scattering index [4] and Ω the rotational speed. The sign of m is coherent with the θ direction defined in Fig. 3.

Such acoustic perturbations travel upstream and downstream with different propagating behaviors depending on the axial wave number k_x. The k_x quantity can be real, the corresponding acoustic mode of which is cut-on, or complex with cut-off mode. Cut-off modes decay as they propagate axially, whereas cut-on waves keep their amplitude unchanged resulting more dangerous for aeromechanical and acoustic implications.

A single spinning lobe generated by the first 2 rows, changes frequency when it is seen in the different frame of reference of the blade-row 3 (refer again to Fig. 3) as follows:

$$\omega_3 = -\omega_2 + m_2(\Omega_3 - \Omega_2) \tag{4}$$

Moreover, a single pressure perturbation also experiences successive scattering when propagating across successive blade-rows. The scattering effect due to a further blade-rows with N_{sr} airfoils generates new sets of rotating perturbations with circumferential order m^{sw} related to the fundamental propagating one m^f by the following relations:

$$m_{sr}^{sw} = m_{sr}^{f} + k_{sr} N_{sr} \tag{5}$$

in which the subscript "sr" stands for scattered row and the superscript "sw" for scattered waves. Scattered waves also change their angular frequency with respect to the fundamental one when analyzed in a different frame of reference where the scattering occurs. For instance, when studying spinning lobe frequencies in the absolute frame of reference (the statoric frame), stator scattering does not alter the fundamental frequency ω^f, while rotor scattering generates scattered perturbations with the following new frequencies:

$$\omega_{sr}^{sw(\mathrm{abs})} = \omega_{sr}^{f(\mathrm{abs})} + k_{sr} N_{sr} \Omega_{sr} \tag{6}$$

Table 1
Rotor-stator-rotor example.

rotor1	$N_1 = 13$	$\Omega_1 = \Omega$
stator1	$N_2 = 10$	$\Omega_2 = 0$
rotor2	$N_3 = 12$	$\Omega_3 = \Omega$

Conversely, in the rotor frame of reference, the stator scattering produces additional rotating lobes with different frequencies.

Referring again to Fig. 3, all the possible scattered waves m_4^{sw} generated by the single (fundamental) propagating perturbation with $m_4^f = m_3$ at the new frequency $\omega_4^f = -\omega_3 + m_3(\Omega_4 - \Omega_3)$ when interacting with blade-row 4, have circumferential orders, in frame of reference 4, equal to:

$$m_4^{sw} = m_4^f + k_4 N_4 \tag{7}$$

with corresponding frequencies in the statoric frame of reference:

$$\omega_4^{sw(\mathrm{abs})} = \omega_4^{f(\mathrm{abs})} + k_4 N_4 \Omega_4 \tag{8}$$

Therefore, it is evident that the scattering phenomenon, due to the interaction of Tyler and Sofrin modes with successive blade-row, generates a number of additional perturbations not immediately detectable and potentially dangerous for all the blade-rows. Such perturbations deserve to be carefully studied during the aeromechanical design verification.

2.3. Interference diagram with acoustic excitation

The interference diagram is widely used to detect possible resonance conditions in both compressors and turbines. Its use is based on the assumptions that the structure is in cyclic symmetric, and the forcing is a rotating pressure perturbation, with an engine order given by the excitation count, that may excite the structure at a space harmonic index, or nodal diameter, equal to the aliased engine order. The coincidence of the excitation frequency and shape of a structural mode is graphically identified in the interference diagram through the well-known "zig-zag" line.

However, a single engine order may include additional spatial contents on top of the aliased engine order, due to different rotor-stator interactions associated to the same time harmonic. Since the additional spatial harmonics may have sufficient amplitude to cause significant blade vibratory responses, it is necessary to capture their presence in the interference diagram with the procedure explained below. A simplified rotor-stator-rotor example with the count expressed in Table 1, and following the conventions defined in Fig. 3, is used as a case study to explain the overall identification process.

With reference to the engine order 10X excitation on *rotor2*, the aliased engine order corresponds to the main interaction detected by the classical use of the interference diagram for *stator1-rotor2* and it would excite the nodal diameter equal to 2:

$$m_3 = N_2 - N_3 = -2 \Rightarrow ND = 2$$

where ND positive sign means that this interaction excites the forward traveling wave mode-shape. Moreover, also the interaction *stator1-rotor1* produces nodal diameter excitations at the engine order 10X on the *rotor1*, that will have an impact also on the spatial content of *rotor2* at the same 10X engine order due to the Tyler-Sofrin modes traveling from *rotor1* to *rotor2*. For example, in the rotor frame of reference, the *rotor1* experiences at the engine order 10X:

$$m_1^a = N_2 - N_1 = -3$$

and

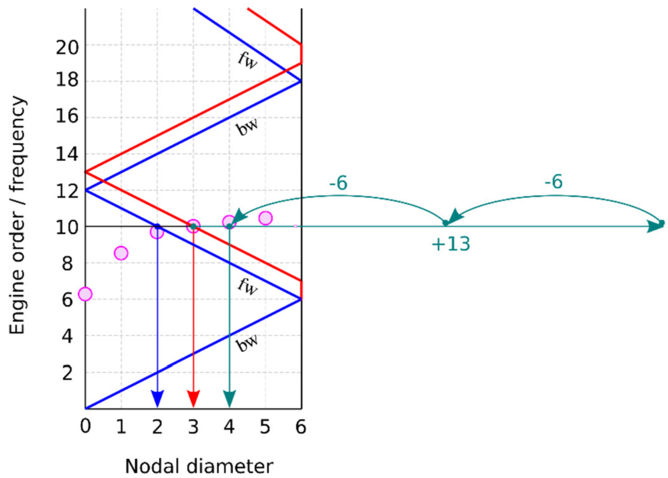

Fig. 4. Suggested use of the interference diagram with acoustic excitations for *rotor2* (the dots represent the mode-shape frequencies). The classical use detects a single $ND = 2$ excitation, while the improved use is able to detect two additional excitations ($ND = 3, 4$). The aliasing phenomenon producing $ND = 4$ excitation is graphically described.

$$m_1^b = N_2 - 2N_1 = -16$$

These two interactions generate acoustic spinning lobes that travel across the *stator1* and merge in the engine order 10X on the *rotor2* and will excite the following forward nodal diameters:

$$m_3^a = m_1^a = -3 \Rightarrow ND = 3$$

$$m_3^b = m_1^b = -16 \xRightarrow{aliasing} ND = 4$$

This last interaction is aliased as a 4 nodal diameter excitation as already explained in Fig. 2.

In the improved use of the interference diagram, the crossings with modes having a spatial harmonic index, or nodal diameter, coincident with the additional spatial content are also considered.

Fig. 4 sketches the sample *rotor2* interference diagram, highlighting a case where the classical use of the interference diagram would detect only the $ND = 2$ excitation, not highlighting any acoustic forcing at the considered speed. However, the horizontal projection of the engine order frequency 10X (that defines the acoustic scattering process described above) matches two modes that are excited by a further circumferential orders of the overall 10X forcing (in this case, $ND = 3$ due to m_3^a, and the aliased $ND = 4$ due to m_3^b) calling for a potential resonant conditions caused by a Tyler-Sofrin mode.

In summary, the recognition of additional resonances excited by Tyler-Sofrin rotor-stator interactions can be done in two steps:

- step 1 (classical use): determination of excitation frequency through the zig-zag line and check the overlap with any mode having harmonic index equal to the aliased engine order
- step 2 (improved use to account for Tyler-Sofrin excitations): horizontal (constant frequency) projection searching for any modes having a circumferential order included in the forcing function at the studied engine order and detectable by the spatial decomposition process described above.

In light of this, the time-spatial decomposition of unsteady forcing at the studied engine order, becomes a key aspect to detect any possible resonance conditions on the interference diagram taking into account both classical and "Tyler-Sofrin" additional crossings.

2.4. Aerodynamic damping derivation

A further key aspect of the forced response analysis concerns the evaluation of the overall damping resulting from the sum of mechanical and aerodynamic contributions necessary to translate vibrations into mechanical stresses. The overall damping is expressed as:

$$\xi = \xi_m + \xi_a \tag{9}$$

Mechanical damping prevails when damping devices based on friction concepts are used. In axial compressors, in absence of sliding surfaces during the bladed disk oscillation, the aerodynamic contribution to the overall damping must not be neglected [15]. For this reason, the overall aeromechanic risk verification process described here includes a procedure to evaluate the aerodynamic damping numerically using the CFD tool described in [13]. The numerical approach is based on non-linear unsteady simulations with vibrating blade-row in traveling wave manner, as usually done for flutter uncoupled analysis. The evaluation of damping has very practical implications when the process is adopted in the framework of a design loop, as it allows to move from the identification of a potential risk to a true mechanical risk. Moreover, the effect of adjacent rows on aerodynamic damping have also been assessed showing a little impact on R7 damping for the mode-shapes under consideration.

To evaluate the aerodynamic damping, the so-called aerodynamic work L is computed by using the following integral quantity:

$$L = \int_t^{t+T} \int_\Sigma (-p)\,\vec{n} \cdot \vec{v_b}\, d\Sigma dt \tag{10}$$

where p is the instantaneous pressure over the blade surface and $\vec{v_b}$ the blade oscillation velocity. Finally, the aerodynamic damping is computed as:

$$\xi_a = \frac{-L}{8\pi E} \tag{11}$$

in which E is the blade average kinetic energy [16]. The derivation of the aerodynamic damping is reported in Appendix A.

2.5. Modal work approach

Finally, the blade-row forced response is computed by a numerical approach based on modal work computation [17]. The approach is valid for resonant conditions and assumes that, at a crossing, the energy associated to the forcing function, extracted by the abovementioned spatial decompositions is equal to the energy dissipated by the overall system damping. Under this assumption, it is possible to compute a scaling factor that can be applied to modal displacements and stresses to obtain the actual displacement and the corresponding oscillating stress. The modal work approach determines the maximum energy transfer of a rotating pressure perturbation, decomposed on blade corresponding points and defined by the circumferential order, applied to the corresponding traveling wave mode-shape defined by the nodal diameter. The search for a maximum value is required by the fact that the phase shift between rotating forcing and mode-shape is unknown. After some algebra (see Appendix B), it can be demonstrated that the scaling factor for the displacements d, and for the stresses, depends on modal force F_m, the total system damping ξ and the square of angular frequency ω as summarized in the following formula (j is the imaginary units):

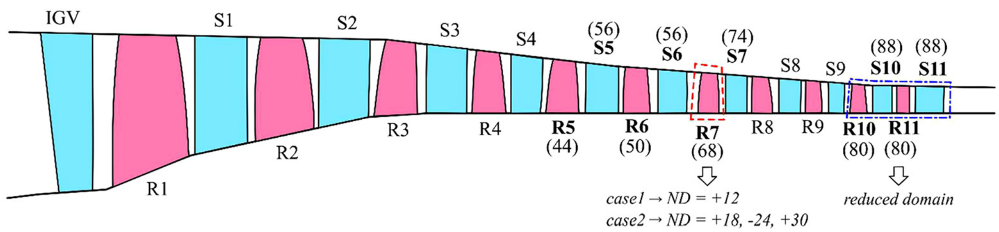

Fig. 5. Compressor meridional view: the rotor under investigation (Rotor 7) is highlighted by a dashed line, while the reduced domain is defined by the dash-dotted line. Blade count is reported in brackets.

$$d = \frac{F_m}{j2\xi\omega^2} \tag{12}$$

Finally, the modal force can be computed by the complex dot product between the conjugate of the modal displacement δ_m^* coming from modal analysis in cyclic symmetry and the aerodynamic forcing F_a spatially decomposed to match the nodal diameter of the mode-shape as follows:

$$F_m = \sqrt{\left[\iint_\Sigma \Im\mathfrak{m}\left[\delta_m^* F_a\right] d\Sigma\right]^2 + \left[\iint_\Sigma \Re\mathfrak{e}\left[\delta_m^* F_a\right] d\Sigma\right]^2} \tag{13}$$

3. Industrial compressor test case

The test data and the corresponding computational approach of the 11-stage axial compressor prototype under investigation here are described by Burberi et al. [13]. The test details and the instrumentation described in [13] allowed a detailed aerodynamic characterization of the multi-stage axial compressor, while this paper tackles the aeromechanic analysis of the same compressor. Fig. 5 shows the meridional view of the overall compressor. In the picture, the rotor under investigation (Rotor 7) is highlighted by the dashed line, and the blade count of adjacent rows concurring on generating the acoustic forcing is reported. The reduced domain, for investigation of the impact of the blade count modification, is also shown in Fig. 5.

3.1. Measurement

All the compressor airfoils were instrumented with strain gages. The Rotor 7 scrutinized in this paper was instrumented with two wire resistance strain gages constructed of platinum/tungsten alloy placed in the positions and orientations shown in Fig. 6. The gages were attached with a thermal spray process, and the grid dimension was 3.18 × 1.57 mm. The uncertainty in the position of the gage was ±0.75 mm, while the uncertainty in the orientation was ±5 deg. The gages were installed on different blades.

3.2. Selection of the case study

In this paper the resonant response of an intermediate rotor stage (Rotor 7) to the engine order excitation of the upstream stator (Stator 6) at different rotational speed will be used as validation data. Two different resonances that showed a repeatable behavior across multiple test instances are used as reference test cases, as summarized in Table 2.

The airfoil count of the rows concurring in generating the acoustic excitation on Rotor 7 are reported in Fig. 5. The Rotor 7 interference diagram computed with the assumptions explained in paragraph 4.1 is shown in Fig. 7. The diagram reports both the classical crossing, and three additional crossings due to acoustic excitations.

The aliased engine order corresponding to the Stator 6 count (56) on Rotor 7 (68) is equal to 12. The *case1* measured resonance is clearly detected by the standard use of interference diagram, as visible by the crossing of the vertical dash-dot line, corresponding to the harmonic index (nodal diameter) of 12, with the *case1* frequency that coincides with one resonant mode described by the large-dots line.

On the contrary, the *case2* measured resonance, although lower in amplitude, is not captured by the classical interference diagram, and it needs further explanations based on the spatial decomposition theory outlined in the previous paragraph, as it does not immediately appear as a risk from the baseline interference diagram.

Observe that, as there are no natural modes with harmonic index equal to the aliased engine order of 12 close to *case2* frequency, the measured response must be due to a mode with a different harmonic index, or nodal diameter. The detailed explanation of the origin of a forcing with higher nodal diameters is done in the paragraph 5.2.2.

Table 2
Reference cases for R7 response validation.

	case1	*case2*
Rotational Speed (N/N_{ref})	0.90	1.00
Normalized Frequency (f/f_{ref})	0.90	1.00
Corrected mass flow ($m_c/m_{c,ref}$)	0.66	1.00
Compressor Inlet Pressure (bar)	0.76	0.40
Overall Pressure ratio (PR/PR_{ref})	0.56	1.00
Most sensitive gage measured response (microstrain) (position and orientation in Fig. 6)	303 (gage1)	85 (gage2)

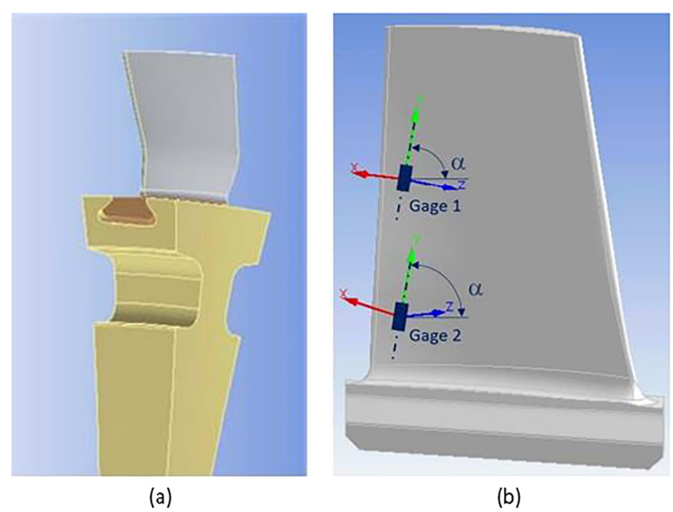

Fig. 6. (a) View of the reference compressor Rotor 7 bladed disk (b) Reference compressor Rotor 7 gages position and orientation (both gages oriented along Y axis).

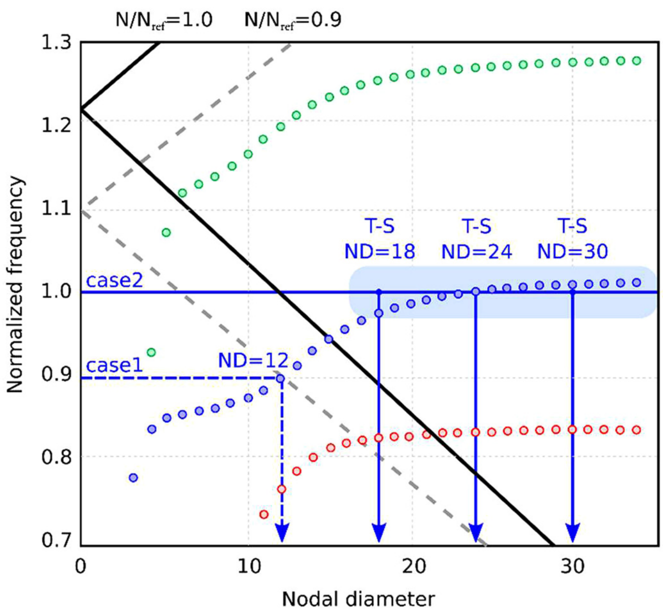

Fig. 7. R7 interference diagram. The improved use detects both classical (*case1*), and acoustic T-S crossings (*case2*).

4. Computational framework

4.1. FEM analysis

The FEM model included a fundamental sector of Rotor 7, comprising the corresponding portion of disk and accounting for cyclic symmetry constraints (see Fig. 6); non-linear contact has been assumed to model rotor-disk interface.

Special attention has been paid to capture the major phenomena the effects on component dynamics of which are well-known: pre-stress, geometrical non-linearities and temperature dependent material properties.

Therefore, the simulation setup consisted of a pre-stressed modal analysis, thereby requiring the stress results coming from the static computation to be considered into the subsequent modal counterpart, acting on the system stiffness matrix. In fact, in gas turbine compressor blades the contribution of the pre-stressed state onto blade dynamics can be significant: the combination of generally high tensile stresses and slender airfoil geometry often leads to measurable variation of blade natural frequencies.

Geometrical non linearities represented the second focus of the static calculation. Again, slender airfoil aero design being operated at high nominal speed can undergo sensible structural deformation – especially when characterized by a certain level of 3D complexity – which tends to straighten the geometry in the radial direction and to reduce bending stresses, thus affecting component eigenvalues by means of the modal pre-stress. Geometrical non linearities play also a second important role in settling the accuracy of the unsteady pressure mapping process. Unsteady pressure distributions coming from CFD calculations usually refer to components under operative condition, thus in *hot* temperature state and subject to static pressure and inertial loads. A quality structural analysis should then be able to correctly predict the shape of the component, like the effect of untwist, once in its operating condition yet starting from its cold shape, usable for production. If good accordance is met, the mapping of hot unsteady pressure onto an initially cold model will also benefit from the accuracy of the map superposition.

Finally, the analysis accounted for material properties variation over operating temperature. As widely known, material Young modulus tends to decrease with increasing temperature, leading to measurable drop of the component natural frequencies.

4.2. CFD analysis

All the CFD computations have been carried out with the TRAF code developed at the University of Florence [18], while the computational setup for the unsteady analysis of the entire compressor may be found in [13].

The TRAF code solves the unsteady Reynolds-averaged Navier-Stokes equations with a finite volume formulation on H-type and O-type structured grids. The discretization of convective fluxes is handled by a 2^{nd} order TVD-MUSCL strategy build on the Roe's upwind scheme, while a central difference scheme is used for the viscous fluxes [19]. The turbulence closure is based on the Wilcox $k-\omega$ model in its high-Reynolds formulation [20].

Unsteady simulations are performed by means of a dual-time stepping technique [21,22,14] with sliding interfaces between adjacent rows and buffer zones at the domain extremities to avoid spurious reflections [23]. Aerodynamic damping computations are also carried out by URANS simulations with moving meshes [15]. The high level of the code parallelization achieved by means of a hybrid openMP/MPI code architecture [24] was exploited to reduce the computational time.

4.3. Forced response analysis

The forced response is computed by means of the theory described in the first part of the paper. Modal analyses of a bladed disk sector in cyclic symmetry have been carried out by means of the FEM ANSYS solver. Natural frequencies and mode-shapes were used to perform aerodynamic damping analyses and modal work assessments.

For the full 11-stage compressor URANS simulation (performed by TRAF code), the time-varying solution was integrated for three complete rotor revolutions to guarantee a periodic solution during the last period. A runtime temporal DFT is activated during the last period of the URANS computations to obtain the time Fourier coefficients of the solution on selected blocks within the domain. Such coefficients are extracted on the blade surface and split up into rotating perturbation with a dedicated post-processing tool to obtain the single forcing functions. The overall computation took 15 days on a Linux cluster using 750 cores.

Aerodynamic damping simulation are performed with the TRAF code on a row vibrating in traveling wave manner and the aerodynamic work is directly computed during the last blade oscillation period.

The forced response is computed by means of the modal work tool which takes as inputs the blade mode-shape, the decomposed forcing functions and the total damping. This allows the computation, on the CFD discretized blade surface, of the scaling factor to be applied to modal displacement and stresses as already described. A near point interpolation strategy is used to transfer blade mode-shape on the CFD blade surface discretization: the choice of CFD discretization ensures a more accurate computation of the modal force.

5. Results and discussion

Unsteady lift results are reported firstly for a reduced domain extracted from the compressor rear block to better highlight key aspects of the proposed methodology like the impact of airfoil count on the rotating forcing spatial decomposition. The comparison with experimental data is presented on Rotor 7 test case as introduced in section 3, where the spatial decomposition theory is applied to determine the proper unsteady pressure component to be applied to compute *case2* forced response.

Table 3
Reduced domain: case definition.

	R10	S10	R11	S11
Case A	80	88	80	88
Case B	76	88	80	88
Case C	80	92	80	88

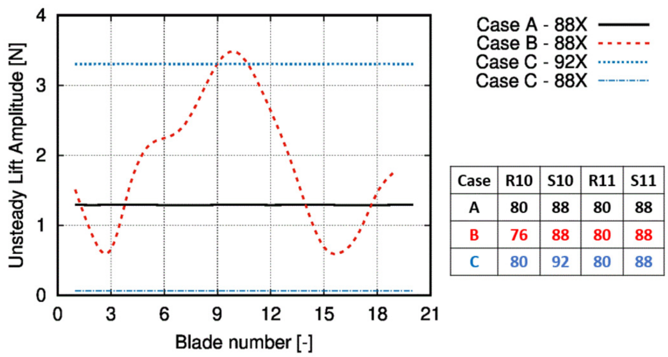

Fig. 8. Unsteady lift amplitude on R10.

5.1. Reduced domain results

The reduced domain, that includes only two compressor final stages to reduce the computational effort from the full compressor computations [13], has been simulated to clarify the observed circumferential distortions of the unsteady lift amplitude at the analyzed engine orders. Table 3 reports the three cases under investigation. Three reduced domain cases have a blade counts divisible by 4, and so for all these cases, a quarter of the wheel has been simulated, leading to a minimum period of a quarter of the rotational period. To obtain a periodic solution 8 minimum periods have been simulated. Each simulation required around 7 days with a number of cores equal to the sum of the reduced domain blade count divided by 4.

Case A corresponds to the baseline case, where rotor and stators rows are characterized by the same blade count, respectively. The R10 blade count of case B is decreased by four with respect to case A, while S10 blade count of case C is increased by four. The variation in the blade number was selected to have in all the cases a common dividend equal to four. This condition allows to perform the CFD unsteady simulations equivalent to full annulus by using only one quarter of the complete annulus, solving all the relevant frequencies and saving computational time and cost.

Fig. 8 shows the variation of the unsteady lift amplitude of R10 as a function of the blade numbering included in the computational domain (1/4 of the entire wheel). The investigated frequency corresponds to the BPF due to the downstream stator row (88X for case A and B, 92X for case C). Case C and A present a common value, while case B, that is characterized by having a different blade count between R10 and R11, shows a circumferential variation of the lift amplitude.

Applying the circumferential DFT to the pressure time Fourier coefficients on the blade surface, the contribution of the different nodal diameters can be separated. The unsteady forces at 88X of case B are composed by the two main contributions which match different nodal diameters: $ND = 12$ is excited by the interaction between R10 and S10, while $ND = 8$ responds to the upstream running wave generated by the Tyler-Sofrin interaction between S10 and R11. The sum of the two unsteady rotating forces at same frequency, but different circumferential patterns, leads to a variation of the amplitude along the circumferential direction. This behavior is easily explained by Fig. 9 and Fig. 10, that show two simplified cases characterized by the overlap of two waves, the first one with the same number of circumferential order (as for case A), and the second one with a different number of m (as for case B).

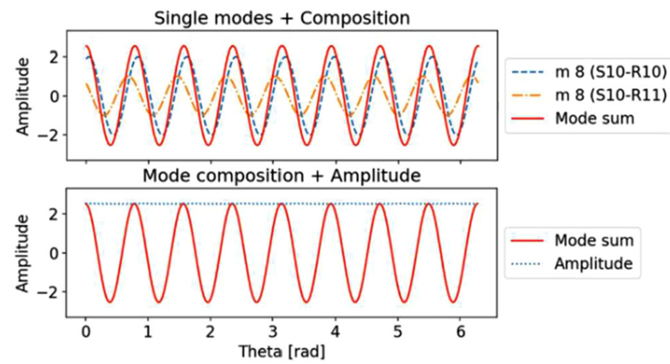

Fig. 9. Overlap of two sinusoidal waves with the same number of nodal diameters.

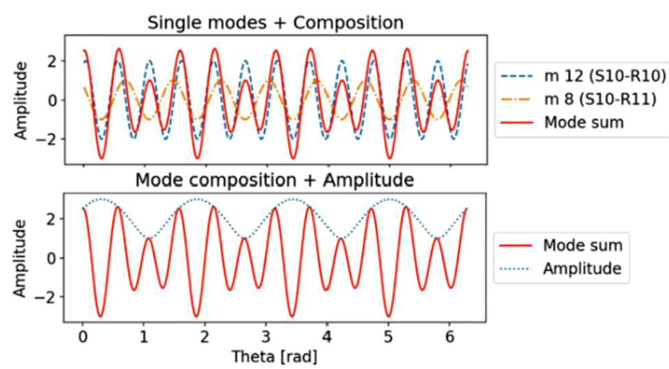

Fig. 10. Overlap of two sinusoidal waves with different number of nodal diameters.

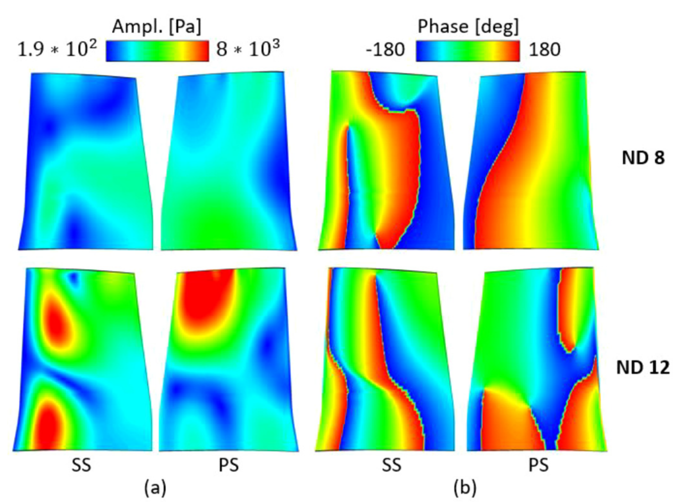

Fig. 11. Case B: Unsteady pressure amplitude (a) and phase (b) from time and space decomposition: EO=88X, ND=8 (top) and ND=12 (bottom) on R10. (For interpretation of the colors in the figure(s), the reader is referred to the web version of this article.)

In the two cases, the final wave composed by the sum of the two contributions present different amplitude trend. Fig. 9 shows a constant amplitude shape since the overlap of two waves with the same m is identical along the circumferential direction, while the sum of two waves with different circumferential pattern varies with the tangential position and determines a non-uniform amplitude distribution, as shown in Fig. 10.

The decomposed unsteady pressure distributions in terms of amplitude and phase for 88X on R10 surface relative to case B are

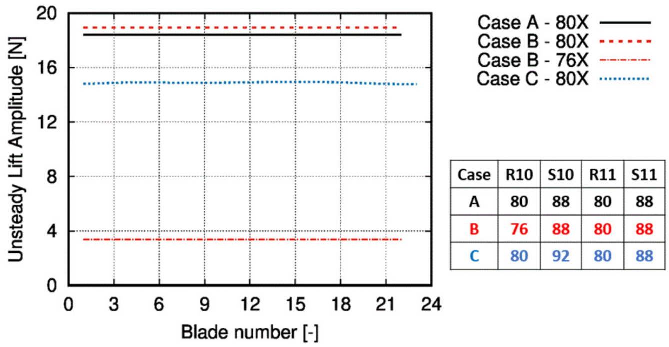

Fig. 12. Unsteady lift amplitude on S10.

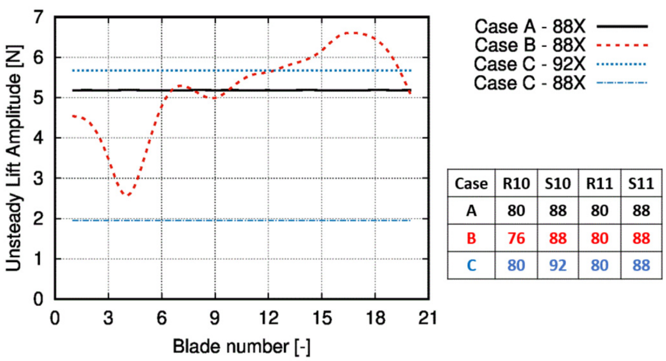

Fig. 13. Unsteady lift amplitude on R11.

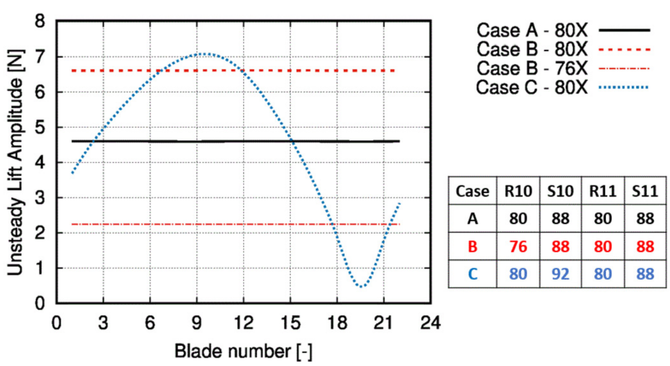

Fig. 14. Unsteady lift amplitude on S11.

shown in Fig. 11. The upper side of the picture corresponds to the contribution that excites $ND = 8$, while the lower side corresponds to $ND = 12$.

Observe that also the unsteady forces at 88X and 92X of case A and case B respectively are composed by the sum of two contributions. Still, they share the same circumferential order and therefore it is not possible to separate the two contributions.

Fig. 12 shows the variation of the unsteady lift amplitude of S10 with the blade number. The trend is constant for case A and B, while case C presents a very slight oscillation due to the very low contribution of the upstream running pressure wave which excites $ND = 8$ generated by the interaction between R11 and S11.

The variation of the unsteady lift amplitude of R11 and S11, shown in Fig. 13 and Fig. 14 respectively, confirms that the tangential distortions occur when the blade-rows in the same frame of reference have a different count (case B for R11 and case C for S11).

The spinning lobes due to Tyler-Sofrin unsteady interactions (mainly acting on $ND = 12$ both for R11 and S11) show a relevant amplitude because they are due to a downstream running wave.

The resulting tangential distortion is clearly visible when the contribute of the Tyler-Sofrin pressure waves has an amplitude comparable to the main interaction, as shown in Fig. 15. Both amplitude and phase plots reveal that $ND = 8$ and $ND = 12$ have quite different shapes that may excite different natural mechanical modes.

In the three cases where the circumferential variation of the unsteady lift amplitude has been observed, the curve shows indicatively a single oscillation.

. Considering that the plot includes only a quarter of the full wheel and the domain is periodic, the circumferential distortions is characterized by four lobes along the full annulus (see the not-parallel lines in Fig. 13 and Fig. 14). The number of circumferential distortions in the unsteady lift is related to the difference of the blade number in the same frame of reference and it is due to the fact that the two rotating waves composing the unsteady forces present the same difference in the number of nodal diameters.

5.2. Overall compressor domain: R7 results

The unsteady computation on the entire axial compressor allows the evaluation of the complete unsteady aerodynamic field and all the excitations generated by the multiple airfoil rows. In particular, the rich frequency spectrum seen by R7 blade-row predicted by the 11-stage unsteady simulation is shown in Fig. 16. The unsteady lift amplitude and the engine orders are reported on y-axis and x-axis respectively. The plot shows multiple points for each engine order and each point corresponds to the unsteady lift amplitude value of a single airfoil constituting the R7 blade-row. All the engine orders that characterize the frequency spectrum show a relevant blade-to-blade variability in terms of unsteady lift amplitude.

As explained in the previous section, the unsteady lift amplitude blade-to-blade variability in a same blade-row is due to the superpositions of two or more rotating unsteady pressure waves that share the same frequency, but different circumferential patterns. Considering that each circumferential order can excite a particular nodal diameter of the blade-row, the circumferential decomposition is therefore necessary for the accurate forced response assessment.

Here, the resonant response of R7 to the engine order excitation of S6 has been investigated. Fig. 17 shows the blade-to-blade variation of unsteady lift amplitude of the BPF 56X on R7.

The amplitude variation between the minimum and maximum value is larger than 100%. This means that the contribution of the different spinning perturbations is not negligible. Applying the circumferential DFT to the unsteady pressure time Fourier coefficients on the blade surfaces, the contribution of the different circumferential order can be finally separated.

Fig. 18 shows the maximum value of the amplitude of the time-space Fourier coefficients on the blade surface decomposed into all the possible m that will excite the NDs of the blade-row for *case2*.

Similar results are observed for the other operating point under investigation described in Table 2 as *case1*.

The sign on the ND is referred to the rotational direction of the spinning perturbation compared with the rotational speed direction, in detail:

- negative values correspond to forward running forcing respect to R7.
- positive values correspond to backward running forcing respect to R7.

The origin of the spinning lobe circumferential orders found from the time-spatial decomposition of the CFD simulation (which will excite the cyclic mode-shapes) of the engine order 56X is ex-

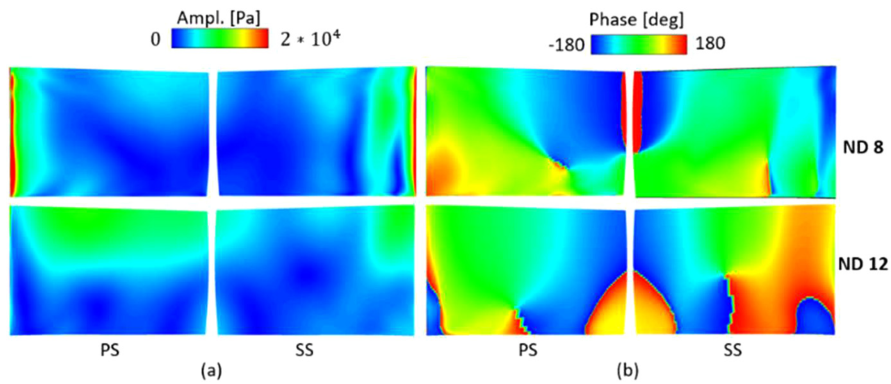

Fig. 15. Unsteady pressure amplitude (a) and phase (b) from time and space decomposition: EO= 88X with ND=8 (top) and ND=12 (bottom) on S11.

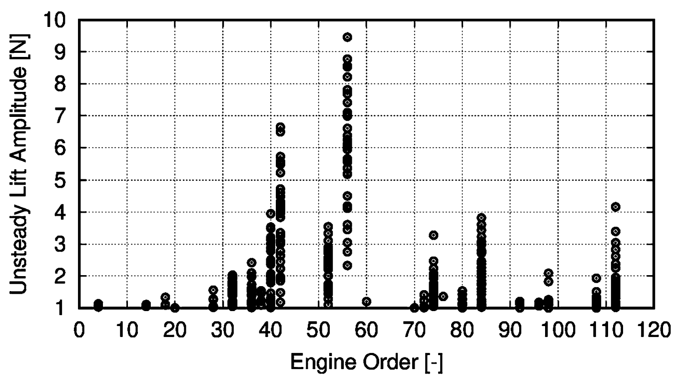

Fig. 16. R7 frequency spectrum (*case2*).

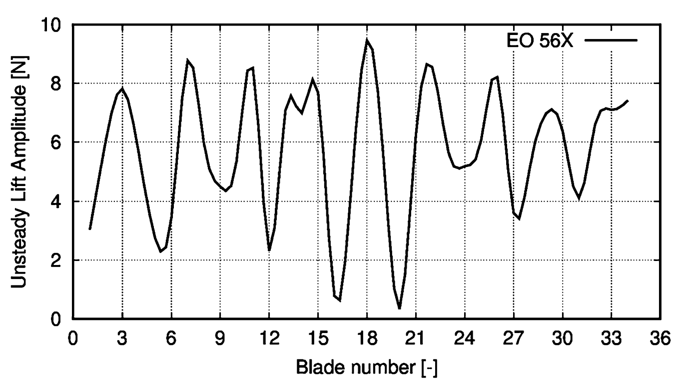

Fig. 17. Unsteady lift amplitude of EO 56X on R7 (*case2*).

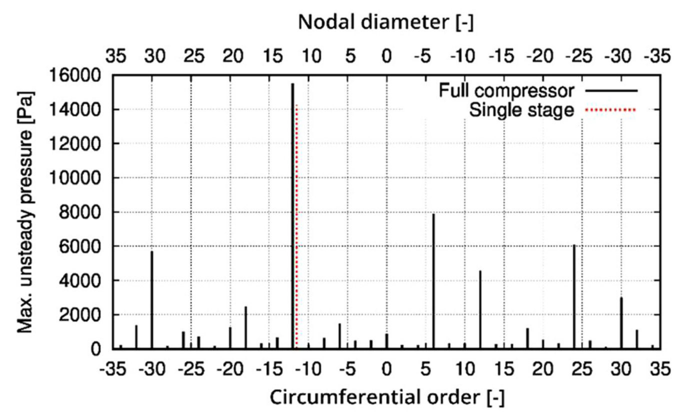

Fig. 18. Maximum unsteady pressure amplitude of EO 56X on R7 blade surface vs. circumferential order and nodal diameter (*case2*).

plained following the theory presented in 2.2. All the perturbation and the excited ND are summarized int the following list:

1. main interaction between S6 and R7

$$m = 56 - 68 = -12 \Rightarrow \mathrm{ND} = 12$$

2. interaction between S6 and R6

$$m = 56 - 50 = 6 \Rightarrow ND = -6$$

3. interaction between S5 and R5

$$m = 56 - 44 = 12 \Rightarrow ND = -12$$

4. interaction between S6 and the second harmonic of R5

$$m = 56 - (50 \times 2) = -44 \xRightarrow{aliased} ND = -24$$

5. interaction between S5 and the rotating distortion due to different count between R6 and R5

$$m = 56 - (50 - 44) = 50 \xRightarrow{aliased} ND = 18$$

6. interaction between S6 and the rotating distortion due to different count between R7 and R6

$$m = 56 - (68 - 50) = 38 \xRightarrow{aliased} ND = 30$$

7. interaction between S6 and the rotating distortion due to different count between the second harmonic of R6 and the second harmonic of R5

$$m = 56 - (68 \times 2 - 50 \times 2) = 30 \Rightarrow ND = -30$$

5.2.1. Classical crossing results (case1)

The validation of the methodology proposed here to evaluate the forced response is performed firstly for *case1* response that is linked to the main interaction (S6- R7), that was shown to be captured by a classical application of the interference diagram (see Fig. 7). The unsteady CFD analysis of the complete compressor domain with boundary conditions coherent with Table 2 was performed to compute the unsteady pressure fluctuation of all the different profiles composing R7 included in the computational model.

Then the spatial decomposition process described in paragraph 2.2 was applied to extract the proper spinning unsteady pressure component that excites the $ND = 12$ rotating in the forward direction. The aerodynamic damping was computed with the numerical procedure detailed in paragraph 2.4, a single row unsteady computation with the R7 blade-row which vibrates following the $ND = 12$ nodal diameter forward rotating mode shape.

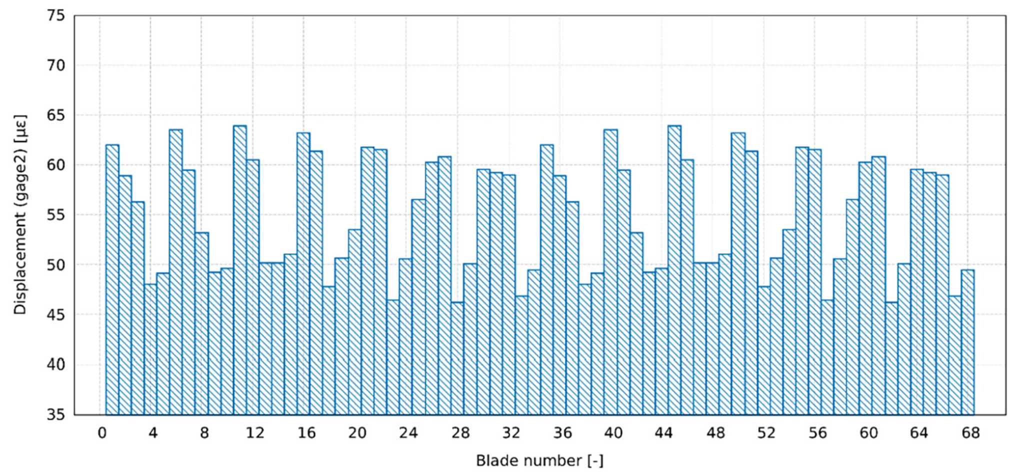

Fig. 19. Composition of the three NDs (−24, +18, +30) for *case2*.

Table 4
Case1 response.

ND	Normalized Frequency	Predicted Q	Predicted Response (gage1)	Measured response (gage1)
12	0.894	594	279.7	303.0

Table 5
Case2 response.

ND	Normalized Frequency	Predicted Q	Predicted response (gage2)	Predicted response (composed, gage 2)	Measured response (gage2)
+18	0.970	742	3.4		
−24	0.998	969	56.0	64	85
+30	1.008	805	7.7		

The comparison between calculated and measured responses on gage1 is summarized in Table 4 and shows a satisfactory agreement. The small difference between the numerical prediction and measurements could be due to uncertainties linked to effective boundary conditions considering that the experimental response was measured during a shut-down transient.

5.2.2. Tyler-Sofrin crossing (case2)

As introduced in section 3, *case2* response requires a more complex explanation. Fig. 18 shows the maximum amplitude of the time-space pressure Fourier coefficients for each circumferential order on the R7 at the 56X engine order from the all compressor computation and the reduced S6-R7 analysis. This comparison with the two-row unsteady computation is important to highlight, not only the rich spectrum content from the full compressor analysis, but also the impact on the main forcing component that excites $ND = 12$ from full compressor simulations. This comparison highlights the appearance of multiple additional spatial content with amplitude indeed lower than the main interaction, but that should be considered to assess the overall blade resonant response risks. The main components and the explanation of their generating mechanism are explained at the end of section 5.2. The additional nodal diameters are highlighted in the R7 interference diagram in Fig. 7 to detect potential resonances in *case2* conditions applying the improved use procedure explained in section 2.3.

Since *case2* excitation frequency is close to the mode natural frequencies for the nodal diameters 18, 24 and 30, the resonant response is computed for all these three cases, by extracting the corresponding unsteady pressure components with the spatial decomposition process on the results of the unsteady CFD analysis of the entire compressor. The modal damping ratio is assumed equal to the aerodynamic damping computed with the presented method for the corresponding mode-shapes. Table 5 compares the predicted and measured *case2* responses.

The interesting result from Table 5 suggests that the $ND = -24$ is most likely responsible for the excitation of the corresponding mode-shape of *case2*. To have a direct comparison with the experimental acquisition at the gage 2 position, the 3 predicted responses have been composed along all the rotor blades (see Fig. 19 and Table 5).

The overall predicted response value is reasonably close to the experimental data, demonstrating that Tyler-Sofrin interactions propagating along the compressor may have enough energy and amplitude to excite airfoils structural modes.

6. Conclusions

The paper illustrated a computational methodology for forced response analysis applicable to multistage axial turbomachinery. The method was successfully applied and validated with the measurements taken on a rotor blade instrumented in the framework of a large experimental campaign on an 11-stage industrial axial compressor.

The proposed methodology is based on the time-spatial decomposition concept of aerodynamic forcing, inherited by the Tyler-Sofrin theory, that allows to leverage full domain unsteady analysis. Very demanding 3D multistage unsteady CFD offers the opportunity to extract the dense and rich spatial harmonic content associated to each Engine Order. The novelty of the proposed approach is that it does allow to identify possible additional excitation sources with respect to the traditional single stator stator-rotor unsteady analysis that considers only the contribution of the main interaction.

The analysis demonstrated that the spatial content associated to the different time harmonics may be originated by Tyler-Sofrin acoustic interactions, usually considered in aeroacoustics analysis only. One of the experimental cases reported in the paper demonstrates that Tyler-Sofrin acoustic interaction may be strong enough to cause measurable structural response levels.

Consequently, an improved use of the interference diagram was proposed to allow the detection of potential additional resonances in the critical design phase knowing the entire forcing spatial content thanks to the proposed decomposition.

The results also demonstrated the advantages stemming from a full, albeit computationally demanding, compressor unsteady CFD simulation that allows capturing all the possible resonances with a forced response coupled CFD/FEA analysis to account for spinning forcing coupled with the corresponding mechanical mode-shapes.

Finally, it was also shown how blade-to-blade variations of lift harmonics within a single blade-row can be justified by the combination of spinning harmonics having a different number of nodal diameters.

Declaration of competing interest

The authors declare that they have no known competing financial interests or personal relationships that could have appeared to influence the work reported in this paper.

Data availability

The data that has been used is confidential.

Acknowledgements

The authors would like to thank Dr. Alberto Scotti Del Greco and Dr. Salvatore Lorusso for several fruitful discussions on the topic of this paper.

Appendix A. Aerodynamic damping derivation

The main mathematical steps to determine the aerodynamic damping are derived for a damped harmonic oscillator in which the damping ratio and the critical damping are:

$$\xi_a = \frac{\zeta}{\zeta_c} \quad \text{and} \quad \zeta_c = 2\sqrt{mk} = 2m\sqrt{\frac{k}{m}} = 2m\omega \tag{14}$$

where m is the mass, k the stiffness and ω the angular frequency. Assuming that the blade-fluid interaction at a vibration amplitude a is due to the generalized force $-\zeta_a \dot{q}$,

$$L = \int_t^{t+T} (-\zeta_a \dot{q})\dot{q}dt = -\frac{1}{2}\zeta_a \omega^2 a^2 T \Rightarrow \zeta_a = \frac{-2L}{\omega^2 a^2 T} \tag{15}$$

The damping coefficient is:

$$\xi_a = \frac{\zeta}{\zeta_c} = \frac{-2L}{2m\omega^3 a^2 T} = \frac{-L}{2\pi m\omega^2 a^2} \tag{16}$$

Finally, for a time-sinusoidal vibration $q = \mathfrak{Re}[\overline{q}e^{i\omega t}]$ having the same amplitude $a = |\overline{q}|$ (with $\overline{q}$ the complex phasor) the blade kinetic energy is:

$$E = \frac{1}{T}\int_t^{t+T} E' dt = \frac{m}{2T}\int_t^{t+T} (\mathfrak{Re}\left[j\omega\overline{q}e^{i\omega t}\right])^2 dt = \frac{1}{4}m\omega^2 a^2 \tag{17}$$

so, the critical damping becomes:

$$\xi_a = \frac{\zeta}{\zeta_c} = \frac{-L}{2\pi m\omega^2 a^2} = \frac{-L}{8\pi E} \tag{18}$$

in which the modal amplitude a is selected to generate small blade vibration amplitude typical of flutter occurrence. Anyway both L and $E \propto a^2$ so, for different small vibrations, the ξ is amplitude independent.

Appendix B. Modal work approach

The main concepts related to the modal work derivation are briefly presented. Let us consider the work per cycle produced by a sinusoidal force during a steady forced vibration. This work must be equal to the energy dissipated during one cycle by the damping force as follows:

$$\pi dF \sin\alpha = \pi\zeta d^2\omega \tag{19}$$

where α is the phase between force and displacement. It may be assumed with sufficient accuracy that this amplitude occurs at resonance condition where $\alpha = \pi/2$, and so:

$$\pi dF = \pi\zeta d^2\omega = 2\pi\xi d^2\omega^2 \tag{20}$$

from which

$$d = \frac{\pi dF}{2\pi\xi d\omega^2} = \frac{F}{2\xi\omega^2} \tag{21}$$

Same conclusion can be drawn for a distributed forcing acting on component modal displacements and leading to the modal force concept as reported in the paper.

References

[1] W.S. Barankievicz, M.D. Hathaway, Effects of stator indexing on performance in a low speed multistage axial compressor, in: International Gas Turbine & Aeroengine Congress & Exhibition, Orlando, FL, 1997.
[2] M. Vahdati, A.I. Sayma, M. Imregun, G. Simpson, Multibladerow forced response modeling in axial-flow core compressors, ASME J. Turbomach. 129 (2007) 412–420.
[3] M. Terstegen, C. Sanders, P. Jenschke, H. Shoenenborn, Rotor-stator interactions in a 2.5-stage axial compressor - Part I: experimental analysis of Tyler-Sofron modes, ASME J. Turbomach. 141 (October 2019) 101002.
[4] J.M. Tyler, T.G. Sofrin, Axial flow compressor noise studies, SAE Transact. 70 (1962) 309–332.
[5] C. Frey, G. Ashcroft, H.P. Kersken, C. Voigt, A harmonic balance technique for multistage turbomachinery applications, in: ASME Turbo Expo, Dusseldorf, 2014.
[6] C. Sanders, M. Terstegen, P. Jeschke, H. Shoenenborn, J.P. Heners, Rotor-stator interactions in a 2.5-stage axial compressor - Part II: impact of aerodynamic modeling on forced response, ASME J. Turbomach. 141 (October 2019) 101008.
[7] M. Baumgartner, F. Kameier, J. Hourmouziadis, Non-engine order blade vibration in a high pressure compressor, in: 12th International Symposium of Airbreathing Engines, Melbourne, Australia, 1995.
[8] F. Figaschewsky, A. Kuehhorn, B. Beirow, Analysis of mistuned forced response in an axial high-pressure compressor rig with focus on Tyler-Sofrin modes, Aeronaut. J. 123 (1261) (2019) 356–377.
[9] L. Zepeng, W. Yanan, Q. Baijie, W. Bi, C. Xuefeng, Experimental investigation of aeroelastic instabilities in an aeroengine fan: using acoustic measurements, Aerosp. Sci. Technol. 130 (2022) 107927.
[10] Y. Xianfei, G. Junnan, Z. Yue, X. Kunpeng, S. Wei, Modeling method of coating thickness random mistuning and its effect on the forced response of coated blisks, Aerosp. Sci. Technol. 92 (2019) 478–488.
[11] P. Tianyu, Y. Zhaoqi, L. Hanan, L. Qiushi, Numerical investigation on the forced vibration induced by the low engine order under boundary layer ingestion condition, Aerosp. Sci. Technol. 115 (2021) 106802.
[12] M. Singh, J.J. Vargo, D.M. Schiffer, J.D. Dello, Safe Diagram - a Design and Reliability Tool for Turbine Blading, Texas A&M University, 1988, Turbomachinery Laboratory.
[13] C. Burberi, V. Michelassi, A. Scotti del Greco, S. Lorusso, L. Tapinassi, M. Marconcini, R. Pacciani, Validation of steady and unsteady CFD strategies in the design of axial compressors for gas turbine engines, Aerosp. Sci. Technol. 107 (12) (2020) 106307.
[14] L. Pinelli, F. Poli, E. Di Grazia, A. Arnone, D. Torzo, A comprehensive numerical study of tone noise emissions in a multistage cold flow rig, in: 19th AIAA/CEAS Aeroacoustics Conference, Berlin, Germany, 2013.
[15] L. Pinelli, F. Vanti, L. Peruzzi, A. Arnone, A. Bessone, C. Bettini, R. Guida, M. Marrè Brunenghi, V. Slama, Aeromechanical characterization of a last stage steam blade at low load operation: Part 2 - computational modelling and comparison, in: ASME Turbo Expo 2020 Turbomachinery Technical Conference and Exposition, London, UK, 2020.
[16] P. Barreca, L. Pinelli, F. Vanti, A. Arnone, Aeroelastic investigation of a transonic compressor rotor with multi-row effects, Energy Proc. 146 (2018) 58–65.

[17] L. Pinelli, F. Lori, M. Marconcini, R. Pacciani, A. Arnone, Validation of a modal work approach for forced response analysis of bladed disks, Appl. Sci. 11 (12) (2021) 5437.

[18] A. Arnone, Viscous analysis of three-dimensional rotor flow using a multigrid method, ASME J. Turbomach. 116 (3) (1994) 435–445.

[19] R. Pacciani, M. Marconcini, A. Arnone, Comparison of the AUSM+-up and other advection schemes for turbomachinery applications, Shock Waves 29 (5) (2019).

[20] D. Wilcox, Reassessment of the scale-determining equation for advanced turbulence models, AIAA J. 26 (11) (1988) 1299–1310.

[21] A. Arnone, M.S. Liou, L.A. Povinelli, Integration of Navier-Stokes equations using dual time stepping and a multigrid method, AIAA J. 33 (6) (1995) 985–990.

[22] L. Pinelli, M. Marconcini, R. Pacciani, P. Gaetani, G. Persico, Computational and experimental study of the unsteady convection of entropy waves within a high pressure turbine stage, ASME J. Turbomach. 143 (9) (September 2021) 091011, https://doi.org/10.1115/1.4050600.

[23] P. Gaetani, G. Persico, L. Pinelli, M. Marconcini, R. Pacciani, Computational and experimental study of hot streak transport within the first stage of a gas turbine, ASME J. Turbomach. 142 (8) (2020) 081002.

[24] F. Poli, M. Marconcini, R. Pacciani, D. Magarielli, E. Spano, A. Arnone, Exploiting GPU-based HPC architectures to accelerate an unsteady CFD solver for turbomachinery applications, in: Proceedings of the ASME Turbo Expo 2022: Turbomachinery Technical Conference and Exposition, vol. 10C: Turbomachinery — Design Methods and CFD Modeling for Turbomachinery; Ducts, Noise, and Component Interactions, Rotterdam, Netherlands, 13–17 June, 2022, 2022.